JOURNAL OF THERMOPHYSICS AND HEAT TRANSFER
Vol. 20, No. 2, April–June 2006

Numerical Simulation of Thermobuoyant Flow with Large Temperature Variation

Masoud Darbandi* and Seyed-Farid Hosseinizadeh†
Sharif University of Technology, 11365-8639 Tehran, Iran

The use of the classical Boussinesq approximation is a straightforward strategy for taking into account the buoyancy effect in incompressible solvers. This strategy is highly effective if density variation is low. However, ignoring the importance of density variation in highly thermobuoyant flow fields can cause considerable deviation from the correct prediction of fluid flow behavior and the accurate estimation of heat transfer rate. In this study, an incompressible algorithm is suitably extended to solve high-density-variation fields caused by strong natural-convection influence. The key point in this research is the way that an ordinary incompressible algorithm is extended to non-Boussinesq-regime applications. The extension results in a unified algorithm capable of solving thermobuoyant flow fields in either a pure incompressible algorithm incorporated with the Boussinesq approximation or an entirely compressible algorithm where the density field is affected by both temperature and pressure fields. The extended algorithm is then verified by solving the benchmark convecting cavity problem at Rayleigh 10^6 and a temperature range of $\epsilon = 0.01$–0.6. The results show that the method can vigorously solve thermobuoyant flow fields with extreme density variation.

Nomenclature

c_p, c_v	=	specific heat constant
F, G, f, g	=	x- and y-momentum components, ρu and ρv, at nodes and cell faces
h	=	enthalpy
k	=	thermal conductivity coefficient
L	=	the enclosure size, Fig. 1
n	=	unit vector in gravitational direction
P, p	=	pressure at nodes and cell faces
Pr	=	Prandtl number
R	=	gas constant
Ra	=	Rayleigh number
S	=	control volume face
s	=	source term
T, t	=	temperature at nodes and cell faces
U, V, u, v	=	velocity components at nodes and cell faces
x, y	=	coordinate directions
α	=	thermal diffusivity
ϵ	=	temperature-difference parameter, Eq. (9)
ϑ	=	magnitude of gravitational field, Eq. (4)
μ	=	viscosity
ν	=	kinematics viscosity
ρ	=	density
σ	=	energy dissipation terms
τ	=	stress tensor components

Subscripts

c	=	cold wall
h	=	hot wall
o	=	old
0	=	the reference state

Superscripts and Accents

$\sim$	=	nondimensionalized parameter
-	=	lagged from previous iteration
*	=	approximate magnitude
$'$	=	correction magnitude

Introduction

BUOYANCY-DRIVEN flows have been investigated for over half a century. Many industrial and nonindustrial applications in heat transfer area have directly or indirectly engaged with research in this field. The importance of the issue has led many researchers to share their contributions to buoyancy-driven study, e.g., Ref. 1. Additionally, to enhance progress in this field of study, several benchmark problems have been defined. These benchmarks can be used to validate the accuracy of newly developed numerical approaches and algorithms. A major part of the past research has been focused on the benchmarks with low temperature gradients where the Boussinesq assumption is definitely valid.[2] For example, one of these is the benchmark solution presented by De Vahl Davis.[3] Unfortunately, there are many different buoyancy-driven flows with large temperature gradients that need to be treated with non-Boussinesq approximations. For example, the fast progress in the field of electronic packaging and the demands to resolve the restrictions caused by the abrupt change of temperature in electronic components promote thermobuoyant research to avoid employing the Boussinesq approximation in treating real thermobuoyant flow fields with extreme density variations. Indeed, the importance and complexity of highly thermobuoyant flow fields have encouraged many researchers to develop suitable numerical methods to treat those flow fields and provide reliable benchmark solutions to be used for verifying the newly developed methods and algorithms. In highly thermobuoyant flows, the compression is mainly the consequence of thermodynamical effects such as heat transfer influences. The classical compressible methods are incapable of solving the Navier–Stokes equations for the low Mach flow fields with high buoyancy influences. On the other hand, the advantages of benefiting the Boussinesq's law in the incompressible algorithm is limited to applications with small temperature gradients or low thermobuoyant influences.[4] Nevertheless, the acoustic phenomena in the flow domain cannot be considered if Boussinesq approximation is assumed.

Different methods and approaches have been developed in the past to solve the flow fields with high density variations or large temperature gradients. Chenoweth and Paolucci[5] numerically solved

Presented as Paper 2004-2459 at the AIAA 37th Thermophysics Conference, Portland, OR, 28 June–1 July 2004; received 27 January 2005; revision received 14 May 2005; accepted for publication 23 May 2005.

*Associate Professor, Dean of Graduate Studies, Department of Aerospace Engineering; darbandi@sharif.edu.

†Ph.D. Candidate, Department of Aerospace Engineering.

the transient Navier–Stokes equations and derived extensive solutions for highly thermobuoyant flows using the ideal gas law and Sutherland's law of transport properties. Choi and Merkle[6] used a time-derivative preconditioning algorithm to solve low-speed thermobuoyant flows. Before developing their preconditioning matrix, they transformed the equations into a viscous set of primary dependent variables. This helped them to circumvent the difficulties originating from the diffusion terms. Yu et al.[7] used a least-squares finite-element method to simulate compressible buoyant flows at low Mach numbers. Their method evades the predicament of the singularity at low Mach number if no special remedy is implemented. Le Quere et al.[8] developed a Chebyshev collocation algorithm to solve natural convection flow with large temperature differences. The thermophysical properties of their working fluid were assumed to vary with temperature according to Sutherland laws. Vierendeels et al.[9] used an explicit third-order discretization for the convection part of the Navier–Stokes equations and a line implicit central discretization for its acoustic and diffusive parts. Their semi-implicit line method is formulated and solved in a multistage form. They treat the low-Mach-number stiffness by a preconditioning technique. Heuveline[10] considers higher-order mixed finite elements with continuous pressures for the computation of stationary compressible flows at low Mach numbers.

Indeed, one efficient approach to solving thermobuoyant flow fields has been the use of compressible–incompressible algorithms; for example, see Ref. 6. In this work, we extend the compressible–incompressible algorithm of Ref. 11 to treat highly thermobuoyant flow fields. This reference utilizes a dual-purpose unified strategy that enables an incompressible algorithm to solve compressible flow using minor modifications. The essence of this SIMPLE-based work is briefly discussed in the *Computational Modeling* section. The algorithm has already shown great performance in treating thermobuoyant flow fields where the Boussinesq approximation is valid.[12] However, in this study, we extend the investigation to high-temperature-gradient fields where the Boussinesq approximation is no longer valid. In this regard, the required formulation is developed and added into the original formulation. Eventually, the extended formulations and algorithm are used to solve highly thermobuoyant flows, excluding and including either the Boussinesq approximation or the Sutherland law. The results obtained provide a vast range of benchmark solutions that can be utilized by the other investigators in the domain of highly thermobuoyant flows.

Considering the points given in the two past paragraphs, this work presents three major contributions to the general field of computational heat transfer and the specific field of thermobuoyant flows with large density variations. One major contribution is to extend a previously unified algorithm capable of treating thermobuoyant flowfields restricted by the Boussinesq approximation to one capable of treating thermobuoyant flowfields with large temperature differences. The second contribution is to enable incompressible algorithms to solve highly thermobuoyant flowfields very accurately in spite of making small modifications in their original incompressible formulations. The third contribution is to provide detailed benchmark solutions in the field of highly thermobuoyant flowfields. They can be used by those who work in the field of computational heat transfer and develop numerical methods capable of solving highly thermobuoyant flowfields. At the end, it should be notified that although the current extended formulations and algorithm are capable of solving highly compressible flows,[11] our main concern in this work has been to study the buoyant flow inside an enclosure which is limited to low Mach compressible flows. Therefore, wherever we refer to the current work as an incompressible–compressible flow solver, we mean an incompressible and low-Mach-compressible flow solver.

Governing Equations

The current algorithm is based on steady-state calculations and does not rely on time-stepping techniques. Hence, if the fluid is assumed to be Newtonian and to obey Stokes's law, the two-dimensional Cartesian form of the governing equations is given by

$$\frac{\partial \mathcal{F}(\psi)}{\partial x}+\frac{\partial \mathcal{G}(\psi)}{\partial y}=\frac{\partial \mathcal{R}(\psi)}{\partial x}+\frac{\partial \mathcal{T}(\psi)}{\partial y}+\mathcal{B} \tag{1}$$

where $\psi=(\{\rho\}, \rho u, \rho v, \rho e)^T$. The convection and diffusion flux vectors and the buoyant source term are written as

$$\mathcal{F}=(\rho u, \rho u^2+p, \rho uv, \rho uh)^T \tag{2a}$$

$$\mathcal{G}=(\rho v, \rho vu, \rho v^2+p, \rho vh)^T \tag{2b}$$

$$\mathcal{R}=(0, \tau_{xx}, \tau_{xy}, \sigma_x-q_x)^T \tag{3a}$$

$$\mathcal{T}=(0, \tau_{yx}, \tau_{yy}, \sigma_y-q_y)^T \tag{3b}$$

$$\mathcal{B}=\left(0, \rho\vartheta n_{\vartheta_x}, \rho\vartheta n_{\vartheta_y}, 0\right)^T \tag{4}$$

where $\hat{n}=n_{\vartheta_x}\boldsymbol{i}+n_{\vartheta_y}\boldsymbol{j}$ is a unit vector in the gravitational direction; that is, $\hat{n}=(0,-1)$ in our model. The energy dissipation terms are $\sigma_x=u\tau_{xx}+v\tau_{xy}$ and $\sigma_y=u\tau_{yx}+v\tau_{yy}$. Also, the stress tensor components are

$$\tau_{xx}=2\mu\frac{\partial u}{\partial x}-\left\{\frac{2}{3}\mu\left(\frac{\partial u}{\partial x}+\frac{\partial v}{\partial y}\right)\right\} \tag{5a}$$

$$\tau_{yy}=2\mu\frac{\partial v}{\partial y}-\left\{\frac{2}{3}\mu\left(\frac{\partial u}{\partial x}+\frac{\partial v}{\partial y}\right)\right\} \tag{5b}$$

$$\tau_{xy}=\tau_{yx}=\mu\left(\frac{\partial u}{\partial y}+\frac{\partial v}{\partial x}\right) \tag{5c}$$

The components of heat flux are given by

$$q_x=-k\frac{\partial t}{\partial x} \qquad q_y=-k\frac{\partial t}{\partial y} \tag{6}$$

To relate the real thermodynamic pressure field to the density and temperature fields, the perfect gas law is used, $p=\rho RT$. This equation closes the system of compressible equations. Alternatively, for the incompressible flow case the equation of state reduces to $\rho=$ constant. The terms inside braces in Eqs. (1–5) vanish in the incompressible limit resulting in a reduced form of the governing equations. Additionally, to be consistent with those who utilize the incompressible Navier–Stokes governing equations to analyze the flow fields with heat transfer, we similarly consider the simple Boussinesq approximation to treat the buoyant term in Eq. (1). This approximation is assumed when we solve the incompressible flow case and enforce $\rho=$ constant. In such an invariant density field, Eq. (4) is replaced with

$$\mathcal{B}=\left[0, \rho_0\vartheta\beta(T-T_0)n_{\vartheta_x}, -\rho_0\vartheta\beta(T-T_0)\, n_{\vartheta_y}, 0\right]^T \tag{7}$$

where ρ_0, T_0, and β represent the reference density and temperature magnitudes and the thermal expansion coefficient, respectively.

Equation (1) incorporated with either Eq. (4) or Eq. (7) provides the required tools to treat both incompressible flow with an invariant density field and compressible flow with density field variation. In the heat transfer literature, it is customary to define a parameter that reflects the difference between the highest and the lowest temperatures in the flowfield. The use of this parameter is essential in flowfields with a large difference between the highest and lowest temperatures in the domain. For example, Fig. 1 shows a two-dimensional square enclosure of length L. As is seen, the left and right walls are maintained at hot and cold temperatures $T_h=T_0(1+\epsilon)$ and $T_c=T_0(1-\epsilon)$, respectively. The two other walls are insulated. The temperature-difference parameter is defined as $\epsilon=(T_h-T_c)/(T_h+T_c)$. This parameter can be included in the Navier–Stokes equations. It can be also introduced into the group of nondimensional numbers, which may be utilized to nondimensionalize the governing equations. Since we study highly thermobuoyant flowfields in the enclosure shown in

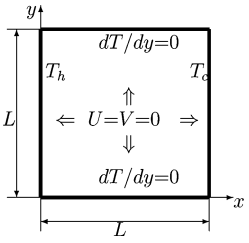

Fig. 1 Typical arrangement for natural convection modeling.

Fig. 1, we rewrite the governing equations in dimensionless form. This helps to have the temperature-difference parameter directly in the governing equations. In this regard, we follow a procedure very similar to one utilized by Chenoweth and Paolucci.[5] In the first stage, we need defining the reference states of the fluid. We specify the reference conditions for the kinematic viscosity ν_0, dynamic viscosity μ_0, thermal conductivity k_0, thermal diffusivity α_0, density ρ_0, specific heat at constant pressure c_{p_0}, and specific heat at constant volume c_{v_0}. Some of these reference properties can be related to each other using general definitions such as thermal diffusivity definition $\alpha_0 = k_0/\rho_0 c_p$. Additionally, the fluid properties can be related to the reference conditions in flow using the equation of state, $P_0 = \rho_0 R T_0$. The reference flow conditions are chosen as $P_0 = 101{,}325$ Pa and $T_0 = 600$ K. The reference velocity and temperature are then defined as

$$U_0 = \alpha_0/L, \qquad T_0 = (T_h + T_c)/2 \tag{8}$$

where U_0 is named the thermal diffusion speed. The reason for choosing the thermal diffusion speed as a reference velocity is first to nondimensionalize the governing equations in terms of the two important Rayleigh and Prandtl numbers instead of the Reynolds number and second to involve the temperature-difference parameter in the nondimensional equations. Using the zero-state reference data, the definition of the temperature-difference parameter yields

$$\epsilon = [(T_h - T_c)/(T_h + T_c)] = \Delta T/2T_0 \tag{9}$$

Considering the definition of ϵ and the chosen reference data, the independent dimensionless Rayleigh and Prandtl numbers are given by

$$Ra = 2\epsilon\vartheta L^3 \big/ \nu_0\alpha_0, \qquad Pr = \nu_0/\alpha_0 \tag{10}$$

In this study, the Rayleigh and Prandtl numbers are considered to be 10^6 and 0.71, respectively. To rewrite the equations in nondimensional form, we have to use nondimensional lengths, areas, and volumes. This is fulfilled by defining

$$\tilde{x} = \frac{x}{L}, \qquad \tilde{y} = \frac{y}{L}, \qquad \widetilde{\mathrm{d}S} = \frac{\mathrm{d}S}{L^2}, \qquad \widetilde{\mathrm{d}\mathcal{V}} = \frac{\mathrm{d}\mathcal{V}}{L^3} \tag{11}$$

where L is the dimension of the chosen enclosure; see Fig. 1. Similarly, the other fluid properties and the flow variables can be nondimensionalized with respect to the reference state. This consideration yields

$$\tilde{u} = u/U_0, \qquad \tilde{v} = v/U_0 \tag{12a}$$

$$\tilde{\rho} = \rho/\rho_0, \qquad \tilde{p} = p \big/ \rho_0 U_0^2, \qquad \tilde{T} = (T - T_c)/(T_h - T_c) \tag{12b}$$

$$\tilde{\mu} = \mu/\mu_0, \qquad \tilde{k} = k/k_0, \qquad \tilde{c}_p = c_p/c_{p_0} \tag{12c}$$

We can use the above definitions to nondimensionalize the momentum components, which will be chosen as the main dependent variables in our algorithm. These components are nondimensionalized to

$$\tilde{f} = \tilde{\rho}\tilde{u} = f/f_0 = \rho u/\rho_0 U_0 \tag{13a}$$

$$\tilde{g} = \tilde{\rho}\tilde{v} = g/f_0 = \rho v/\rho_0 U_0 \tag{13b}$$

Using the above nondimensional definitions, the nondimensional form of the governing equations can be written as

$$\frac{\partial \tilde{f}}{\partial \tilde{x}} + \frac{\partial \tilde{g}}{\partial \tilde{y}} = 0 \tag{14}$$

$$\frac{\partial(\tilde{u}\tilde{f})}{\partial \tilde{x}} + \frac{\partial(\tilde{v}\tilde{f})}{\partial \tilde{y}} = -\frac{\partial \tilde{p}}{\partial \tilde{x}} + Pr\left(\frac{\partial \tilde{\tau}_{xx}}{\partial \tilde{x}} + \frac{\partial \tilde{\tau}_{xy}}{\partial \tilde{y}}\right) + \frac{Ra\ Pr}{2\epsilon}\tilde{\rho} n_{\vartheta_x} \tag{15}$$

$$\frac{\partial(\tilde{u}\tilde{g})}{\partial \tilde{x}} + \frac{\partial(\tilde{v}\tilde{g})}{\partial \tilde{y}} = -\frac{\partial \tilde{p}}{\partial \tilde{y}} + Pr\left(\frac{\partial \tilde{\tau}_{yx}}{\partial \tilde{x}} + \frac{\partial \tilde{\tau}_{yy}}{\partial \tilde{y}}\right) + \frac{Ra\ Pr}{2\epsilon}\tilde{\rho}\, n_{\vartheta_y} \tag{16}$$

$$\frac{\partial(\tilde{c}_p\tilde{t}\tilde{f})}{\partial \tilde{x}} + \frac{\partial(\tilde{c}_p\tilde{t}\tilde{g})}{\partial \tilde{y}} - \frac{\partial}{\partial \tilde{x}}\tilde{k}\frac{\partial \tilde{t}}{\partial \tilde{x}} - \frac{\partial}{\partial \tilde{y}}\tilde{k}\frac{\partial \tilde{t}}{\partial \tilde{y}} = \text{L.O.T.} \tag{17}$$

As is observed, the temperature-difference parameter ϵ is directly involved in the governing equations now. L.O.T. indicates the low-order terms in the energy equation, which are calculated from

$$\text{L.O.T.} = \frac{\mu_0^2}{c_p\rho_0^2(PrL)^2(T_h - T_c)}\left(\tilde{u}\frac{\partial \tilde{p}}{\partial \tilde{x}} + \tilde{v}\frac{\partial \tilde{p}}{\partial \tilde{y}}\right) - \frac{\tilde{\rho}\tilde{v}\vartheta L}{c_p(T_h - T_c)} + \frac{\tilde{\mu}\mu_0^2}{c_p\rho_0^2 Pr\, L^2\,(T_h - T_c)}\left[\frac{4}{3}\tilde{\theta}^2 + \tilde{\omega}^2 + 4\left(\frac{\partial \tilde{u}}{\partial \tilde{y}}\frac{\partial \tilde{v}}{\partial \tilde{x}} + \frac{\partial \tilde{u}}{\partial \tilde{x}}\frac{\partial \tilde{v}}{\partial \tilde{y}}\right)\right] \tag{18}$$

where $\tilde{\theta} = \partial\tilde{u}/\partial\tilde{x} + \partial\tilde{v}/\partial\tilde{y}$ and $\tilde{\omega} = \partial\tilde{v}/\partial\tilde{x} - \partial\tilde{u}/\partial\tilde{y}$. Additionally, the dimensionless forms of the stress terms given in Eqs. (15) and (16) are very similar to those given in Eq. (5). For example, $\tilde{\tau}_{xx}$ is given by

$$\tilde{\tau}_{xx} = 2\tilde{\mu}\frac{\partial \tilde{u}}{\partial \tilde{x}} - \left\{\frac{2}{3}\tilde{\mu}\left(\frac{\partial \tilde{u}}{\partial \tilde{x}} + \frac{\partial \tilde{v}}{\partial \tilde{y}}\right)\right\} \tag{19}$$

As was mentioned in the Introduction, the viscosity and thermal conductivity of the fluid can be assumed either constant or variable in a compressible algorithm. On the other hand, we need to consider the variation of these fluid properties in treating highly thermobuoyant flowfields. The effect of temperature dependency on viscosity has been reported in the related literature. This is done using either an exponential law for liquids (where the viscosity decreases with temperature increase) or Sutherland's law for gases (where the viscosity increases with temperature increase).[5,13,14] Following the strategy taken by past investigators, we also use the Sutherland law to approximate the required viscosity and thermal conductivity variations. This law assumes that

$$\mu(T)/\mu_{\text{ref}} = (T/T_{\text{ref}})^{1.5}(T_{\text{ref}} + T_s)/(T + T_s) \tag{20}$$

$$k(T) = \mu(T)c_p/Pr \tag{21}$$

where $T_{\text{ref}} = 273^\circ$K, $T_s = 110.5^\circ$K, $\mu_{\text{ref}} = 1.68 \times 10^{-5}$ kg m^{-1}s^{-1}, $c_p = \gamma R/(\gamma - 1) = 1004.5$ J kg^{-1} K^{-1}, $\gamma = 1.4$, $R = 287$ J kg^{-1} K^{-1}, and $Pr = 0.71$. Chenoweth and Paolucci[5] indicate that the accuracy of the Sutherland law degrades rapidly above $\epsilon = 0.6$ for air.

Domain Discretization

Our two-dimensional solution domain is discretized in a staggered-grid manner.[15] This means that the domain is divided into a number of quadrilateral control volumes that do not overlap each other and fully cover the solution domain; see Fig. 2. In this arrangement, nodes are located at the centers of control volumes and are the locations of pressure field computation. They are shown by circles in Fig. 2 and labeled by upper case letters such as P, E, W, N, and S. However, velocities are computed at the faces of control volumes. These faces are labeled by lower case letters such as e, w, n, and s. This dual grid for dependent variable computation on

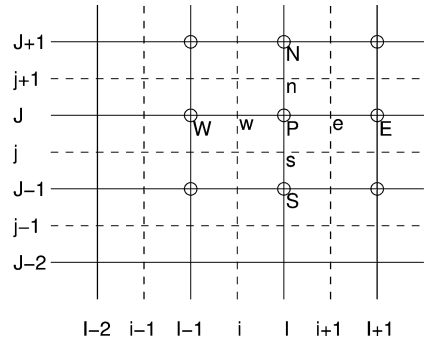

Fig. 2 Staggered-based domain discretization and nomenclature.

two adjacent grids is known as a staggered grid arrangement. To simplify the notations in *Computational Modeling*, we use capital letter subscripts I and J to enumerate the main grid lines that pass nodal points in x- and y-directions, respectively, and lower case subscripts of i and j to enumerate the grid lines that pass cell faces in the x- and y-directions, respectively.

In the current algorithm, the upper case letters F, G, P, and T are chosen as the dependent variables of the solution algorithm. The first two unknowns represent $F = \rho U$ and $G = \rho V$.

Computational Modeling

To be consistent with the compressible research in the field, we also treat the nondimensional governing equations in this section. The integration of a suitable rearrangement of the governing equations, that is, Eqs. (14–17), over an arbitrary control volume yields

$$\int_{\tilde{S}} (\tilde{f}\,\boldsymbol{i} + \tilde{g}\,\boldsymbol{j}) \cdot \mathrm{d}\widetilde{\boldsymbol{S}} = 0 \tag{22}$$

$$\int_{\tilde{S}} \left[\{\tilde{u}\}\tilde{f}\,\boldsymbol{i} + \{\tilde{v}\}\tilde{f}\,\boldsymbol{j} + \tilde{p}\,\boldsymbol{i} - Pr\frac{\tilde{\mu}}{\tilde{\rho}}\left(\frac{\partial \tilde{f}}{\partial \tilde{x}}\,\boldsymbol{i} + \frac{\partial \tilde{f}}{\partial \tilde{y}}\boldsymbol{j}\right)\right] \cdot \mathrm{d}\widetilde{\boldsymbol{S}} = \frac{Pr\,Ra}{2\epsilon} n_{\vartheta_x} \int_{\tilde{\mathcal{V}}} \tilde{\rho}\,\mathrm{d}\widetilde{\mathcal{V}} + \bar{\tilde{s}}^x \tag{23}$$

$$\int_{\tilde{S}} \left[\{\tilde{u}\}\tilde{g}\,\boldsymbol{i} + \{\tilde{v}\}\tilde{g}\boldsymbol{j} + \tilde{p}\boldsymbol{j} - Pr\frac{\tilde{\mu}}{\tilde{\rho}}\left(\frac{\partial \tilde{g}}{\partial \tilde{x}}\,\boldsymbol{i} + \frac{\partial \tilde{g}}{\partial \tilde{y}}\,\boldsymbol{j}\right)\right] \cdot \mathrm{d}\widetilde{\boldsymbol{S}} = \frac{Pr\,Ra}{2\epsilon} n_{\vartheta_y} \int_{\tilde{\mathcal{V}}} \tilde{\rho}\,\mathrm{d}\widetilde{\mathcal{V}} + \bar{\tilde{s}}^y \tag{24}$$

$$\int_{\tilde{S}} \left[\{\tilde{c}_p \tilde{f}\}\tilde{t}\,\boldsymbol{i} + \{\tilde{c}_p \tilde{g}\}\tilde{t}\boldsymbol{j} - \tilde{k}\frac{\partial \tilde{t}}{\partial \tilde{x}}\,\boldsymbol{i} - \tilde{k}\frac{\partial \tilde{t}}{\partial \tilde{y}}\boldsymbol{j}\right] \cdot \mathrm{d}\widetilde{\boldsymbol{S}} = \int_{\tilde{\mathcal{V}}} [\mathrm{L.O.T.}]\,\mathrm{d}\widetilde{\mathcal{V}} \approx 0 \tag{25}$$

Integration over the area and volume of each cell is indicated by S and $\mathcal{V}$, respectively. In addition, $\mathrm{d}\boldsymbol{S}$ is an outward vector normal to the surfaces of the control volume. All the variables in braces are the nonlinear parts of the equations, which in turn need to be linearized suitably. In SIMPLE-based procedures, the transport equations other than the momentum equations, such as the energy equation, are treated individually after the set of continuity and momentum equations is solved. This is why we concentrate more on the momentum and continuity equations rather than the other transport equations in the rest of our modeling.

Following preceding work in the field, we have also assumed zero influence of the dissipation terms on the solution. As is accepted, the order of magnitude of the integral on the right-hand-side of Eq. (25) is negligible. The $\bar{\tilde{s}}^x$ in Eq. (23) and $\bar{\tilde{s}}^y$ in Eq. (24) are the source terms that automatically appear in our derived formulations.[11] They consist of two parts. First, they include the additional diffusion terms in the compressible equations, that is, the terms inside braces in Eq. (5). Second, they include the terms that are generated after the nonlinear diffusion terms are linearized with respect to the chosen dependent variables. This linearization enforces the density gradient terms into $\bar{\tilde{s}}^x$ and $\bar{\tilde{s}}^y$ source terms. The proper consideration of these two aspects in our derivations determines the source terms in the right-hand-side of Eqs. (23) and (24). These source terms are derived from

$$\bar{\tilde{s}}^x = \int_{\tilde{S}} Pr\,\frac{\tilde{\mu}}{3}\left\{\left(\frac{\partial \tilde{u}}{\partial \tilde{x}} - 2\frac{\partial \tilde{v}}{\partial \tilde{y}}\right)\boldsymbol{i} + 3\frac{\partial \tilde{v}}{\partial \tilde{x}}\boldsymbol{j}\right\} \cdot \mathrm{d}\widetilde{\boldsymbol{S}} - \int_{\tilde{S}} Pr\frac{\tilde{\mu}\tilde{u}}{\tilde{\rho}}\left(\frac{\partial \tilde{\rho}}{\partial \tilde{x}}\,\boldsymbol{i} + \frac{\partial \tilde{\rho}}{\partial \tilde{y}}\,\boldsymbol{j}\right) \cdot \mathrm{d}\widetilde{\boldsymbol{S}} \tag{26}$$

$$\bar{\tilde{s}}^y = \int_{\tilde{S}} Pr\,\frac{\tilde{\mu}}{3}\left\{\left(\frac{\partial \tilde{v}}{\partial \tilde{y}} - 2\frac{\partial \tilde{u}}{\partial \tilde{x}}\right)\boldsymbol{i} + 3\frac{\partial \tilde{u}}{\partial \tilde{y}}\boldsymbol{j}\right\} \cdot \mathrm{d}\widetilde{\boldsymbol{S}} - \int_{\tilde{S}} Pr\,\frac{\tilde{\mu}\tilde{v}}{\tilde{\rho}}\left(\frac{\partial \tilde{\rho}}{\partial \tilde{x}}\,\boldsymbol{i} + \frac{\partial \tilde{\rho}}{\partial \tilde{y}}\,\boldsymbol{j}\right) \cdot \mathrm{d}\widetilde{\boldsymbol{S}} \tag{27}$$

As is observed, the first integrations represent additional diffusion terms of the compressible part of equations. However, the second integrations are additional density gradients generated after linearizing the nonlinear incompressible diffusion terms with respect to the chosen dependent variables. The bar over $\bar{s}$ means it is explicitly estimated from the known values of the last iteration. As is expected, these source terms vanish in the incompressible limit.

At this stage, we need to develop an algorithm to solve the discretized governing equations in order to obtain the magnitudes of the unknown dependent variables including F, G, P, and T. We choose the algorithm developed by Darbandi and Schneider.[16] They extended an analogy between the incompressible and compressible governing equations in order to solve the flow at all speeds on collocated grids in a fully implicit manner. Darbandi and Hosseinizadeh[11] extended the analogy to semi-implicit algorithms on a staggered grid arrangement. They show that a compressible flow can be easily solved using a pure incompressible algorithm. They use the dimensional form of the governing equations and consider neither the energy equation nor the buoyancy effect in their extended formulations. According to their derivations, a suitable integration of Eq. (1), excluding the energy equation and the buoyancy terms, results in

$$\int_S (f\,\boldsymbol{i} + g\,\boldsymbol{j}) \cdot \mathrm{d}\boldsymbol{S} = 0 \tag{28}$$

$$\int_S \left[\{u\}f\boldsymbol{i} + \{v\}f\boldsymbol{j} + p\,\boldsymbol{i} - \nu\frac{\partial f}{\partial x}\,\boldsymbol{i} - \nu\frac{\partial f}{\partial y}\,\boldsymbol{j}\right] \cdot \mathrm{d}\boldsymbol{S} = \bar{s}_o^x \tag{29}$$

$$\int_S \left[\{u\}g\boldsymbol{i} + \{v\}g\,\boldsymbol{j} + p\boldsymbol{j} - \nu\frac{\partial g}{\partial x}\,\boldsymbol{i} - \nu\frac{\partial g}{\partial y}\,\boldsymbol{j}\right] \cdot \mathrm{d}\boldsymbol{S} = \bar{s}_o^y \tag{30}$$

where the right-hand-side source terms are derived from

$$\bar{s}_o^x = \int_S \frac{\mu}{3}\left\{\left(\frac{\partial u}{\partial x} - 2\frac{\partial v}{\partial y}\right)\boldsymbol{i} + 3\frac{\partial v}{\partial x}\boldsymbol{j}\right\} \cdot \mathrm{d}\boldsymbol{S} - \int_S \mu\frac{u}{\rho}\left(\frac{\partial \rho}{\partial x}\,\boldsymbol{i} + \frac{\partial \rho}{\partial y}\,\boldsymbol{j}\right) \cdot \mathrm{d}\boldsymbol{S} \tag{31}$$

$$\bar{s}_o^y = \int_S \frac{\mu}{3}\left\{3\frac{\partial u}{\partial y}\,\boldsymbol{i} + \left(\frac{\partial v}{\partial y} - 2\frac{\partial u}{\partial x}\right)\boldsymbol{j}\right\} \cdot \mathrm{d}\boldsymbol{S} - \int_S \mu\frac{v}{\rho}\left(\frac{\partial \rho}{\partial x}\,\boldsymbol{i} + \frac{\partial \rho}{\partial y}\,\boldsymbol{j}\right) \cdot \mathrm{d}\boldsymbol{S} \tag{32}$$

Further, they show that the proper treatment of Eqs. (29) and (30) results in two sets of algebraic equations which can be separately solved to estimate approximate value of F^* and G^* unknowns. These

equations are given by

$$a'_{i,J}F^*_{i,J} = \sum a'_{nb}F^*_{nb} + \left(P^*_{I-1,J} - P^*_{I,J}\right)A'_{i,J} + b'_{i,J} + \bar{s}^x_{o,i,J} \quad (33)$$

$$a'_{I,j}G^*_{I,j} = \sum a'_{nb}G^*_{nb} + \left(P^*_{I,J-1} - P^*_{I,J}\right)A_{I,j} + b'_{I,j} + \bar{s}^y_{o,I,j} \quad (34)$$

where a', b', and A' are explained shortly. Reference 11 shows that Eqs. (33) and (34) can be equivalently solved to obtain U^* and V^* fields when the flow is incompressible. Under incompressible conditions, the source terms given in Eqs. (31) and (32) vanish and Eqs. (33) and (34) can easily be devided by a constant density. The resulting equations are then ready to be solved for U^* and V^* fields without altering a', b', and A'.

In a similar manner, the general form of Eqs. (23) and (24) are suitably treated on the velocity cells. These treatments result in two sets of algebraic equations that can be separately solved to estimate approximate values of $\tilde{F}^*$ and $\tilde{G}^*$ unknowns. These treatments yield

$$a_{i,J}\tilde{F}^*_{i,J} = \sum a_{nb}\tilde{F}^*_{nb} + \left(\tilde{P}^*_{I-1,J} - \tilde{P}^*_{I,J}\right)A_{i,J} + b_{i,J} + \bar{\bar{s}}^x_{i,J} \quad (35)$$

$$a_{I,j}\tilde{G}^*_{I,j} = \sum a_{nb}\tilde{G}^*_{nb} + \left(\tilde{P}^*_{I,J-1} - \tilde{P}^*_{I,J}\right)A_{I,j} + b_{I,j} + \bar{\bar{s}}^y_{I,j} \quad (36)$$

where $a_{i,J}$ and $A_{I,j}$ are the nondimensional cell face areas at the east (or west) and south (or north) of the u-control volume, respectively. Similarly, $b_{i,J}$ and $b_{I,j}$ indicate the source terms in the x- and y-momentum equations, respectively. The values of the coefficients $a_{i,J}$, $a_{I,j}$, $b_{i,J}$, $b_{I,j}$, and a_{nb} are determined after a proper choice of the convection–diffusion model such as upwind, hybrid, and QUICK schemes. In this work, we have chosen the second-order QUICKER scheme to calculate those coefficients.[17] All the velocity components which appear in the preceding coefficients are calculated using the updated velocities taken from the preceding iteration. In the present algorithm, if a pressure field, say $\tilde{P}^*$, is guessed, the system of equations given in Eqs. (35) and (36) can be solved for the subsequent momentum components, $\tilde{F}^*$ and $\tilde{G}^*$. In fact, this strategy is a guess-and-correct tactic which is entirely analogous to an algorithm named SIMPLE, semi-implicit method for pressure-linked equations.[15] The next step is to provide an appropriate procedure to calculate the unknown pressure field.

Although the incompressible continuity equation does not involve any pressure term, it can be used as a complementary equation to obtain a better estimate or prediction of the pressure field. Versteeg and Malalasekera[18] show that the continuity equation can be converted to a pressure correction equation. We similarly develop a pressure correction equation in terms of the chosen $\tilde{P}$ variable. This equation is given by

$$a_{I,J}\tilde{P}'_{I,J} = a_{I+1,J}\tilde{P}'_{I+1,J} + a_{I-1,J}\tilde{P}'_{I-1,J} + a_{I,J+1}\tilde{P}'_{I,J+1} + a_{I,J-1}\tilde{P}'_{I,J-1} + b_{I,J} \quad (37)$$

where $a_{I,J} = a_{I+1,J} + a_{I-1,J} + a_{I,J+1} + a_{I,J-1}$. The *primes* indicate the required corrections to correct the *stars*. This equation provides a tool to estimate the pressure correction field, $\tilde{P}'_{I,J}$, at all pressure cell centers. The next is to correct the preceding approximate values of the dependent variables using the derived pressure correction magnitude. The correction yields

$$\tilde{P} = \tilde{P}^* + \tilde{P}' \quad (38)$$

$$\tilde{F}_{i,J} = \tilde{F}^*_{i,J} + d_{i,J}(\tilde{P}'_{I-1,J} - \tilde{P}'_{I,J}) \quad (39)$$

$$\tilde{G}_{I,j} = \tilde{G}^*_{I,j} + d_{I,j}(\tilde{P}'_{I,J-1} - \tilde{P}'_{I,J}) \quad (40)$$

where $d_{i,J} = A_{i,J}/a_{i,J}$ and $d_{I,j} = A_{I,j}/a_{I,j}$.

The next step in the SIMPLE procedure is to solve the other discretized transport equations, such as the energy transport equation. For example, in a very similar manner, the treatment of the energy equation, Eq. (25), on a pressure cell yields

$$a_{I,J}\tilde{T}^*_{IJ} = \sum a_{nb}\tilde{T}^*_{nb} + b_{I,J} \quad (41)$$

where a and b are determined as before. In the final stage, we may need to update the secondary dependent variables such as nonconstant fluid properties; see Eqs. (20) and (21). For example, if the density field is considered as a secondary dependent variable, it will be updated right at this stage. In a compressible algorithm, the density is updated using the equation of state. For the incompressible case, the density does not need updating.

By the end of this procedure, one iteration has been completely fulfilled. However, if the residuals are not low enough at the end of this iteration the procedure is repeated for another iteration. Using the last iteration outputs, the inputs for the next iteration are approximated using

$$\tilde{P}^* = \tilde{P}, \qquad \tilde{F}^* = \tilde{F}, \qquad \tilde{G}^* = \tilde{G}, \qquad \tilde{T}^* = \tilde{T} \quad (42)$$

One more step at this stage is to ensure global mass conservation in Eq. (37), the continuity equation.[9] In this regard, the new pressure field in Eq. (42) is updated using the conservativeness factor, which is derived from

$$m_f = \frac{\text{theoretical initial mass in the enclosure}}{\text{current total mass in the enclosure}} \quad (43)$$

This factor is further utilized to correct the pressure field. The correction yields

$$\tilde{P}^* = m_f\tilde{P}^* \quad (44)$$

Compared with the solutions presented in Ref. 19, this correction numerously improves the accuracy of the solutions in treating the thermobuoyant flow fields with high temperature-difference parameter magnitude.

As is observed, the procedure in our extended algorithm consists of solving the three systems of algebraic equations given by Eqs. (35–37), correcting the approximate magnitudes of dependent variables through Eqs. (38–40), and updating the dependent variables for the next iteration, Eq. (42). This procedure is independent of the choice of incompressible or compressible assumptions. This implies that the two compressible and incompressible algorithms are essentially the same except for the magnitudes of the extra source terms on the right-hand side of Eqs. (35) and (36). Indeed, the $\bar{\bar{s}}^x$ and $\bar{\bar{s}}^y$ automatically vanish in the incompressible limit and do not normally need any further treatment. Based on the discussion given under Eq. (34), it is evident that the above extended procedure equally works to treat both incompressible and compressible thermobuoyant flow fields.

Results and Discussion

To investigate the performance and accuracy of the extended algorithm, the upright square convecting cavity is chosen as the benchmark problem. This test has been the object of a previous comparison exercise for incompressible flow solvers, which normally practice the Boussinesq approximation.[1,3] The geometry of a square convecting cavity model and its thermal and flow boundary conditions are seen in Fig. 1. The top and bottom walls of the cavity are insulated and the side walls are maintained at constant but different hot and cold temperatures T_h and T_c. The velocity components are zero on all walls. All the results are obtained at Rayleigh number 10^6 but assuming different temperature-difference parameter magnitudes ϵ; see Eq. (9). The grid resolution utilized has been 300×300 in all tests. The reason for this choice of grid is given later. Once more, it is important to note that the flow inside the enclosure performs large density variation due to significant temperature variations if ϵ is large enough. The results are illustrated based on considering three different purposes in this section. First, we assume an invariant density field and solve Eqs. (33) and (34) supported by the Boussinesq approximation given in Eq. (7). In this case, the buoyant terms are included in b' in the right-hand-side of these equations. Second, we consider a compressible domain where the density field obeys the equation of state for the perfect gas and solve Eqs. (35) and (36), which support the non-Boussinesq approximation given in Eq. (4). Third, similarly to the second purpose, we

solve the thermobuoyant flow field using Eqs. (35) and (36) without implementing the Boussinesq approximation. These equations are further incorporated with the variable fluid property assumptions given in Eqs. (20) and (21). The results attributed to these three approaches are referred as incompressible, constant property, and variable property cases, respectively.

Figures 3–5 provide the details of velocity fields inside the enclosure using $\epsilon = 0.01$, 0.4, and 0.6. In these figures, we intend to show the performance of our algorithm in solving flow fields with different buoyant force influences. Each figure consists of two or four subfigures. They represent U (and F) and V (and G) velocity (and momentum component) distributions at $X = 0.5$ and $Y = 0.5$, that the centerlines in the enclosure, respectively. Figure 3 provides the results of three approaches at $\epsilon = 0.01$. In this case, the temperature variation is sufficiently low within the solution domain. This low temperature variation results in low density variation. Additionally,

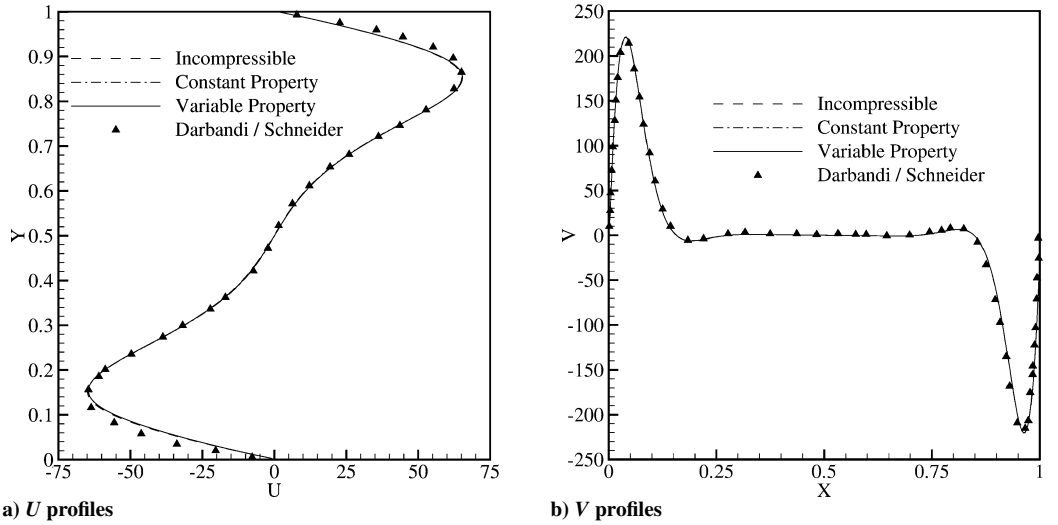

a) *U* profiles **b) *V* profiles**

Fig. 3 Centerline velocity profiles in the cavity and comparison with the incompressible solutions of Darbandi and Schneider,[20,21] $\epsilon = 0.01$.

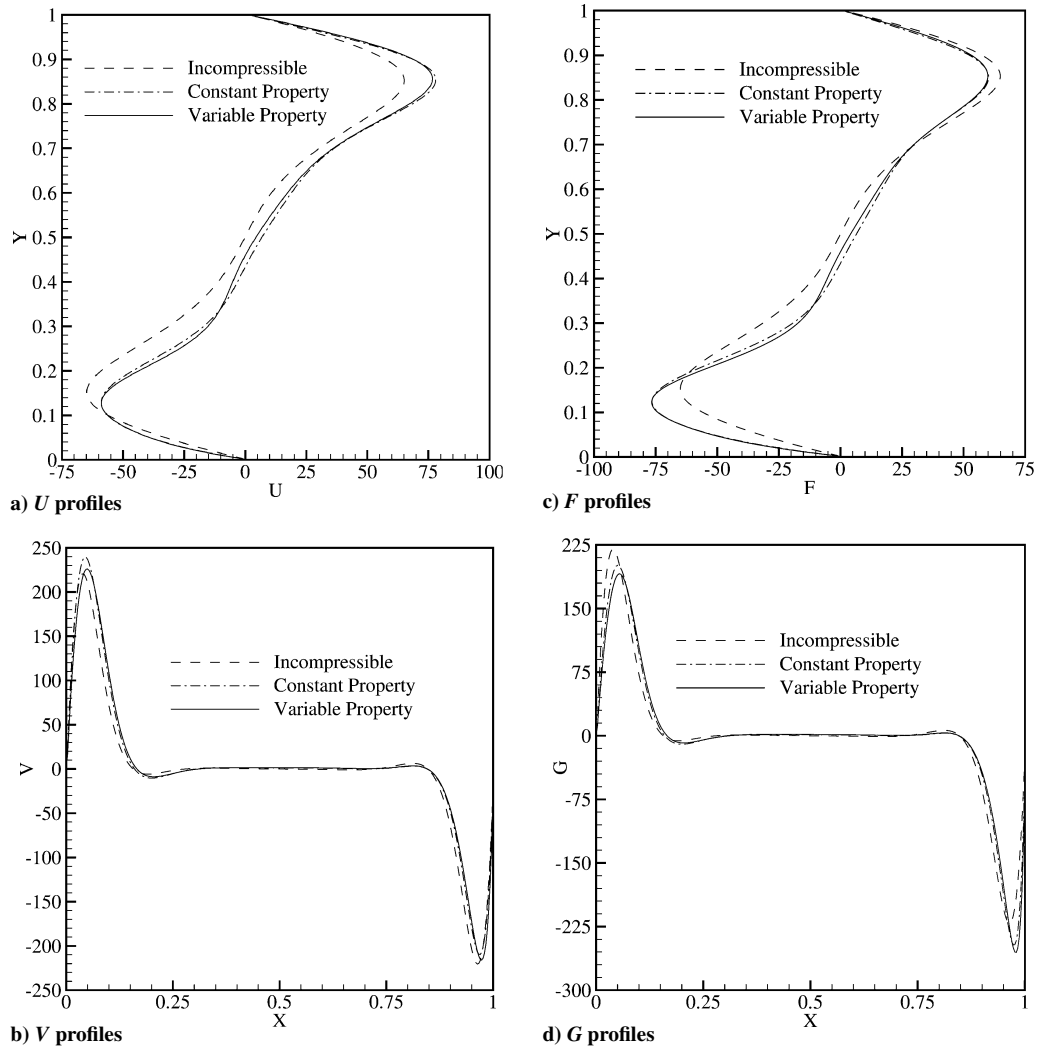

a) *U* profiles **c) *F* profiles**

b) *V* profiles **d) *G* profiles**

Fig. 4 Distributions of velocity and momentum components on the centerlines of the convecting cavity, $\epsilon = 0.4$.

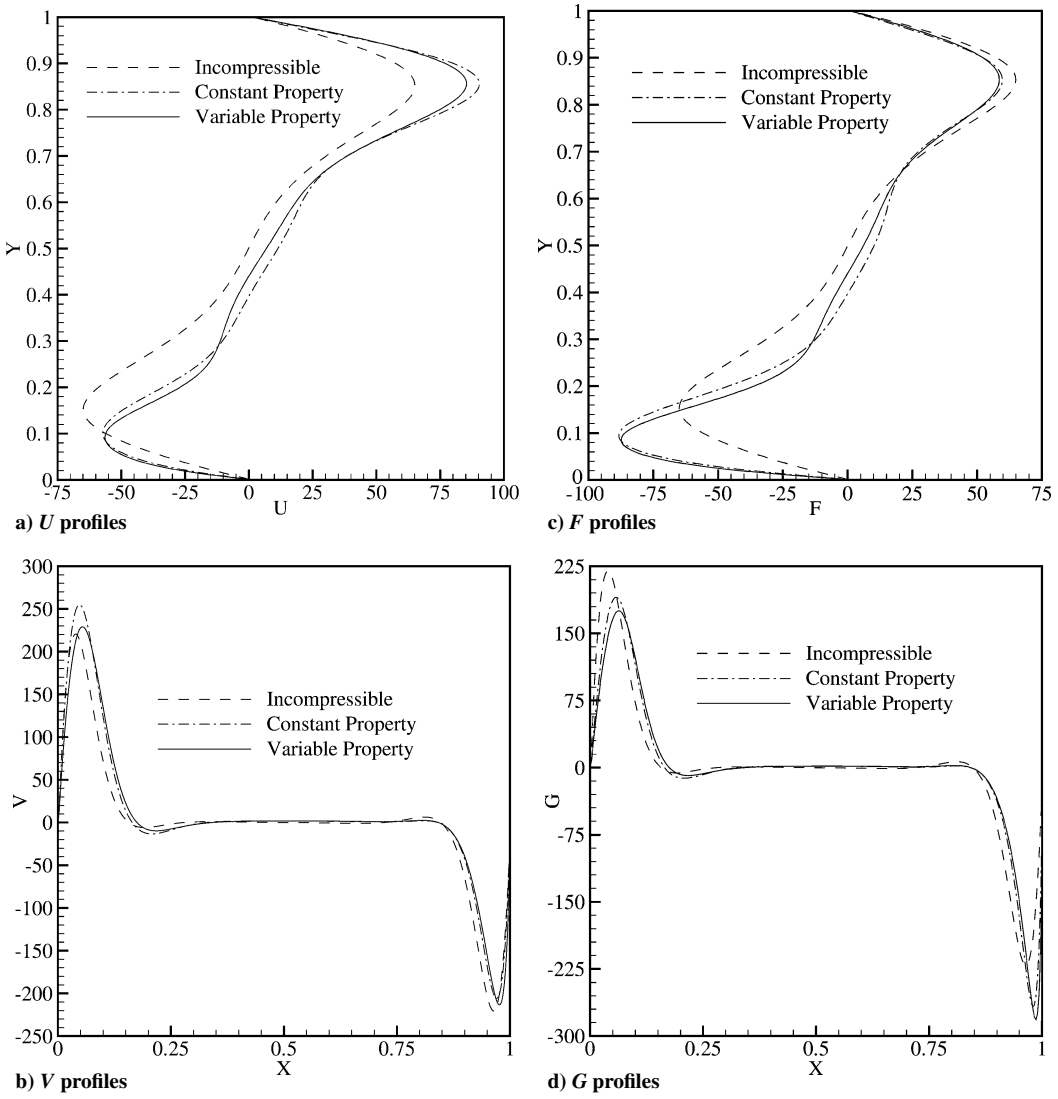

Fig. 5 Distributions of velocity and momentum components on the centerlines of the convecting cavity, $\epsilon = 0.6$.

a low variation in temperature causes little variation in fluid properties. As is observed, there are no major and minor differences among the results of three chosen approaches. They are essentially identical. To validate the solution accuracy, the details of the current results are compared with the available results reported in other references. Darbandi and Schneider[20,21] use a collocated finite-volume-based finite-element method to solve the Navier–Stokes equations in the thermal enclosure. In the former reference, they solve the problem using their own compressible–incompressible algorithm assuming the Boussinesq approximation. The primary object of their research has been to launch an all-speed flow algorithm capable of solving thermobuoyant flow fields. They solve the enclosure problem only at low ϵ and do not implement a variable-fluid-property assumption. Similarly to the results of the current work, there is no major or minor differences between their compressible and incompressible results. In the latter reference, they launch a new method capable of inserting the thermobuoyant weight implicitly into the convection–diffusion model. This effectively improves the performance of their algorithm. Figure 3 indicates that the current results are in good agreement with those of the references. As is seen, both of the references and the current work predict symmetrical solutions with respect to $X = 0.5$ and $Y = 0.5$ axes. Unfortunately, the authors were not able to find any other reliable benchmark solutions that present the U and V velocity profiles inside the enclosure. Fortunately, there are a few benchmark works which report the magnitudes of maximum U and V velocity profiles at the centerlines of the cavity and where these maxima occur. Table 1 compares the current results with those of Refs. 3 and 22. Hortmann et al.[22] extend a finite-volume multigrid

Table 1 Quantitative comparison of current solution with other available benchmark solutions

	U_{max} (diff%)	V_{max} (diff%)	Nu_{max} (diff%)	Nu_{avg} (diff%)
De Vahl Davis[3]	64.63	219.36	17.925	8.800
Present	65.09	220.89	17.610	8.853
	(0.60)	(0.69)	(1.76)	(0.60)
Hortmann et al.[22]	64.834	220.473	17.54	8.826
Present	65.09	220.89	17.610	8.853
	(0.39)	(0.19)	(0.40)	(0.31)

procedure to obtain accurate solutions for the natural convection inside the cavity. They refine grid as low as 640×640 and claim that their results seem to be accurate to within 0.01%. In addition to the maximum velocity magnitudes, the table separately provides the difference percentage between the current results and those of both references. The current results are very close to the benchmark solution and the percentage of difference is very small.

Similarly to Fig. 3, Fig. 4 presents the U and V velocity profiles at $\epsilon = 0.4$. The figure also presents the momentum component distributions, that is, F and G flux terms, at the centerlines of the cavity. This is to evaluate the weight of density variation in a domain with large temperature differences. This figure generally resembles that a higher magnitude of the temperature-difference parameter has caused a higher variation of density within the enclosure. In contrast to the results shown in Fig. 3, the incompressible assumption is not capable of predicting the flow field behavior adequately. It is very

important to note that the incompressible algorithm is not affected by the magnitude of ϵ at all and the results at this chosen ϵ are the same as at $\epsilon = 0.01$. The incompressible solution is not altered as long as the Rayleigh number is constant. As is observed in this figure, the solutions are slightly different than the incompressible case. The increase is more pronounced for the U and F profiles than the V and G profiles. A careful exploration of Fig. 4 indicates that a variable property assumption is relatively important at $\epsilon = 0.4$. As is observed, the differences between the results obtained by including and excluding the fluid property variation are significant in some part of the solution domain. The figure also indicates that the solutions are asymmetric with respect to the cavity centerlines. To the knowledge of the current authors, there is no sound reference in the literature to report the details of flow field solutions at $\epsilon < 0.6$. However, Emery and Lee[23] investigate the effects of fluid property variation in a square cavity and similarly report more asymmetry in solution if the property variation is included in the formulations.

Figure 5 illustrates the mid velocity and momentum components at $\epsilon = 0.6$. Comparing the solutions at $\epsilon = 0.6$ with those at $\epsilon = 0.01$ and 0.4 indicates that a higher magnitude of temperature-difference parameter has caused a more dominant density variation in the domain and, consequently, remarkable differences between the results obtained using the three categorized approaches. Several conclusions can be concluded by exploring Fig. 5. First of all, the incompressible solution fails to provide reliable solutions at this higher ϵ. Evidently, the use of incompressible algorithm for solving highly thermobuoyant flowfields is not wise.[2] Second, the difference between the results of two compressible approaches is surely considerable at this ϵ. In contrast to Fig. 4, the differences are clearly observed in the entire solution domain now. These observation simply implies that constant fluid property considerations certainly result in inaccurate solution in high thermobuoyant flow fields.

Figure 6 displays the Nusselt distributions on the hot and cold walls of the cavity using $\epsilon = 0.01, 0.2, 0.4$, and 0.6. Generally speaking, comparing each subfigure with the equivalent ϵ case in Figs. 3–5 ensures that the differences among the three chosen approaches in predicting the Nusselt distribution are very similar to those in predicting the velocity profiles. For example, Fig. 6a shows that there are no major or minor differences among the results of three approaches when $\epsilon = 0.01$. In this case, all the solutions are absolutely symmetric. Figures 6b–6d indicate that the deviation from the incompressible solution increases as ϵ increases from 0.2 to 0.6. In contrast to the results obtained for the velocity profiles, the Nusselt distributions seem to be more sensitive to ϵ change. Comparing Figs. 6c and 6d with the corresponding cases in Figs. 4 and 5 also indicates that the inclusion or exclusion of the fluid property variation can considerably affect the heat transfer calculations even at smaller ϵ. Evidently, the asymmetry in the solution is more pronounced in the Nusselt distributions than in the velocity profiles. As was mentioned before, the authors were not able to find any benchmark solution to validate the obtained Nusselt distributions at either incompressible or low ϵ cases. However, Table 1 provides the current average Nusselt magnitudes in the incompressible case and compares them with those reported by the other incompressible

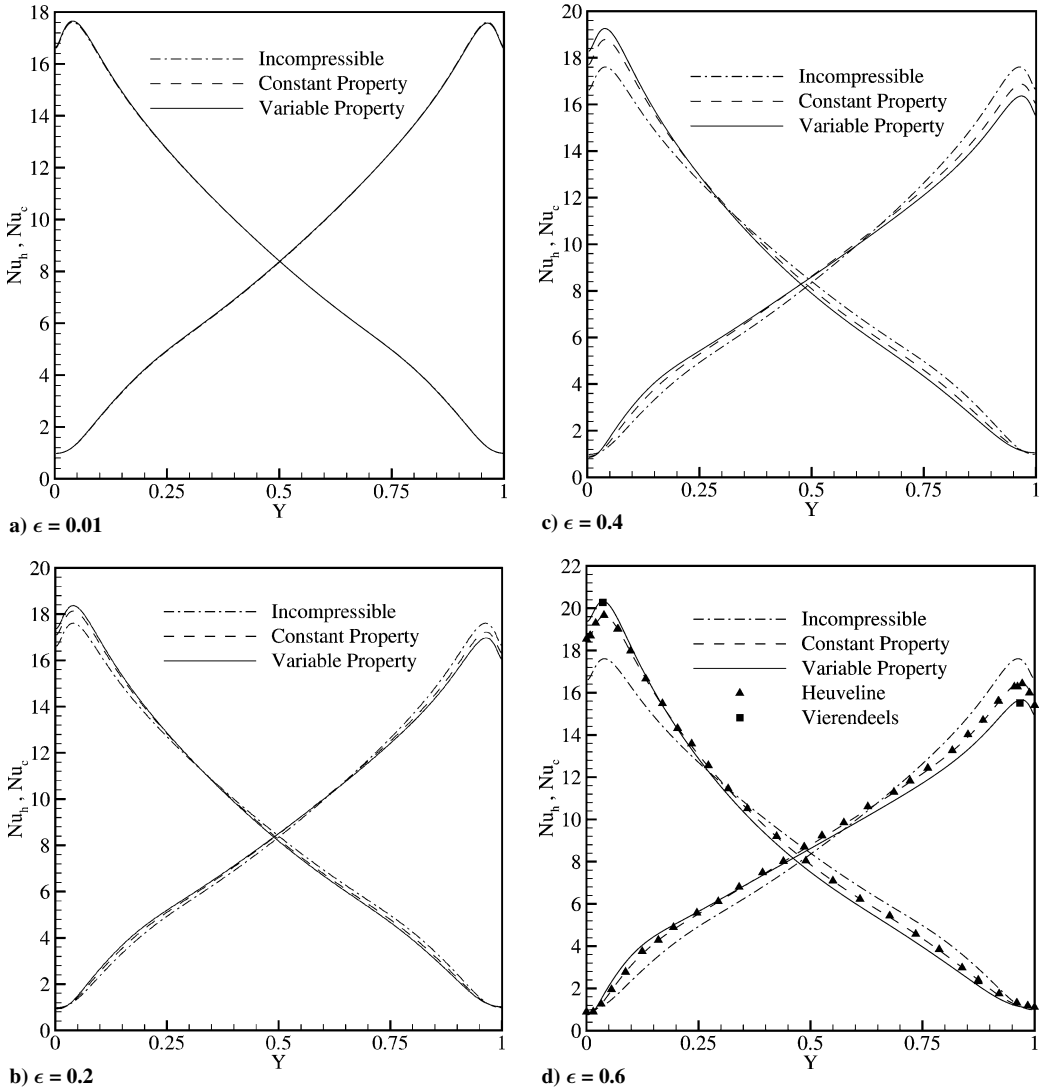

Fig. 6 Nusselt number distributions on the cold and hot walls of the enclosure using different temperature-difference parameters and comparison with those of Vierendeels et al.[9] and Heuveline.[10]

thermobuoyant workers. In this table, the maximum and average Nusselt number magnitudes are compared with those of benchmark workers. There is excellent agreement with the benchmark results in the incompressible limit.

Few references are available that report the Nusselt distributions at $\epsilon = 0.6$. Figure 6d compares the current Nusselt number distributions with those reported by Heuveline[10] and Vierendeels et al.[9] Heuveline[10] solves the convecting enclosure using a compressible algorithm with and without consideration of fluid property variation. We do not insert his constant-property solution because the results display full symmetry with respect to the y-axis. In other words, the behavior of his results is very similar to the results of our incompressible or low-ϵ cases. Alternatively, we have illustrated the variable-property results reported by the reference; see Fig. 6d. As observed, the results of its variable-property solution agrees well with the results of our constant property solution. Nothing to say except that the reference has mistakenly reported the constant property solution instead of the variable property solution. Vierendeels et al.[9] also investigated the convecting cavity problem at large ϵ. They measured the maximum magnitudes of the Nusselt number and their locations on hot and cold walls. The magnitudes are inserted into Fig. 6d using a solid square symbol. As observed, there is excellent agreement between our variable property solution and those of benchmark data. This is an indication of the great accuracy of the current work and inaccuracy of the results given by Ref. 10. Irrespective of the uncertainty in the accuracy of the solutions given by Ref. 10, two major points can be deduced from others' solutions. First, there is asymmetry in the solution. Very similarly to the current results, the asymmetry is more pronounced for the variable-property solution than for the constant-property solution. Second, very similarly to the current results, the Nusselt number on the hot wall (the cold wall) increases (decreases) when the solution is switched from constant-property to the variable-property assumption. Chenoweth and Paolucci[5] indicate that the variable-property may not result in reliable solutions for air if $\epsilon > 0.6$. This is why we do not demonstrate the results at larger ϵ; otherwise, the developed algorithm shows no instability in treating higher thermobuoyant flows as well.[24]

Indeed, the lack of reliable solutions in this field of study has led experts on thermobuoyant fields to improve the situation by performing side activities. For example, a comprehensive study of the current convecting cavity at $Ra = 10^6$ with $\epsilon = 0.6$ has been the topic of a conference organized by INRIA in Proquerolles, France in June 2004. The contributions of the participants have been suitably collected and published as benchmark solutions for low-Mach-number solvers.[24] Similarly to Table 1, we take the opportunity and

Table 2 Quantitative comparison of current compressible solutions with a few other solutions from Ref. 24

	Vierendeels	Dabbene	Beccantini	Heuveline	Darbandi
$\overline{Nu}_h$ [a]	8.860	8.864	8.860	8.860	8.880
$\overline{Nu}_c$ [a]	8.860	8.862	8.860	8.860	8.880
P_{max}/P_0 [a]	0.856	0.857	0.856	0.856	8.856
$\overline{Nu}_h$ [b]	8.687	8.692	8.687	8.689	8.715
$\overline{Nu}_c$ [b]	8.687	8.686	8.675	8.686	8.715
P_{max}/P_0 [b]	0.924	0.926	0.925	0.925	0.923

[a]Constant property case. [b]Variable property case.

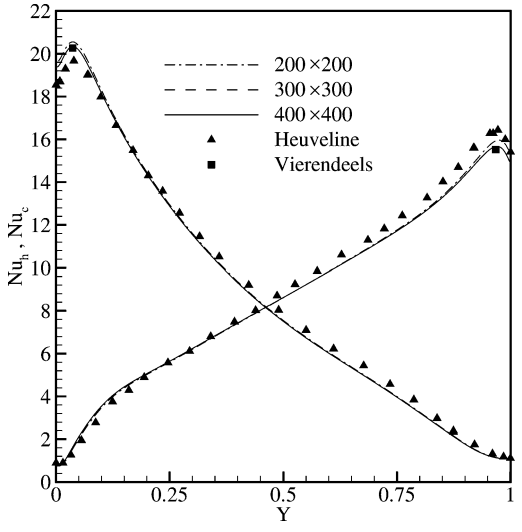

Fig. 7 Results of mesh-independent study, $\epsilon = 0.6$.

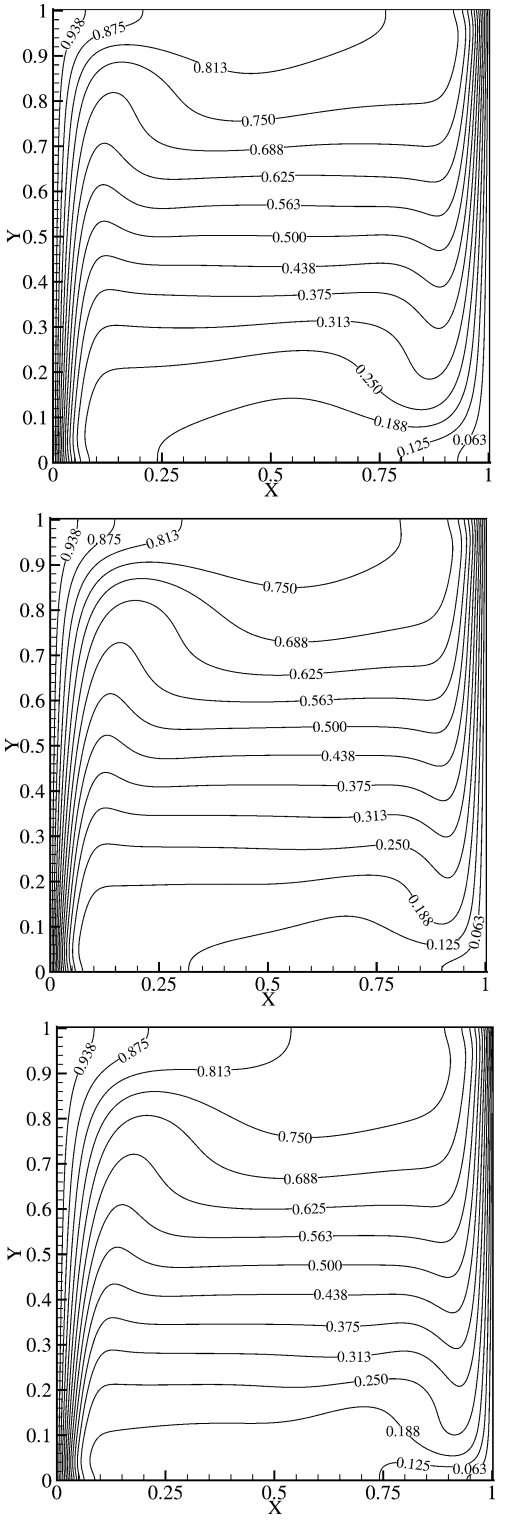

Fig. 8 Isotherms in the convecting cavity using incompressible (top) and compressible without (middle) and with (bottom) fluid property variations, $\epsilon = 0.6$.

quantify our compressible solutions using the solutions reported in Ref. 24. Table 2 provides a vast range of comparisons between the current solutions and those of a few other numerical workers in Ref. 24. The comparison is shown for two key parameters, the average Nusselt numbers on the hot and cold walls and the maximum pressure ratio in the compressible cavity. The table shows that both the constant property and variable property considerations result in reliable solutions comparable with the results of other workers.

To show further the grid independency of the current results, Fig. 7 presents the Nusselt distributions on the hot and cold faces of the cavity using three grid resolutions of 200×200, 300×300, and 400×400. The figure indicates that the numerical diffusion is not significant in our solutions using different grid resolutions. As was mentioned in the *Computational Modeling* section, it is because we employ a second-order scheme in our formulation. The calculations show that the maximum local cell Peclet numbers are around 20–25 in our test cases. They are 20.8 in incompressible case. However, assuming $\epsilon = 0.6$, they are 24.7 and 22.5 for cavities with constant and variable property choices, respectively. In this figure, the current results have been compared with the data of Vierendeels et al.[9] and Heuveline.[10] We have only presented the results of variable property case in this figure. As was mentioned before, the numerical solution of Heuveline is not sufficiently accurate. The figure shows that there

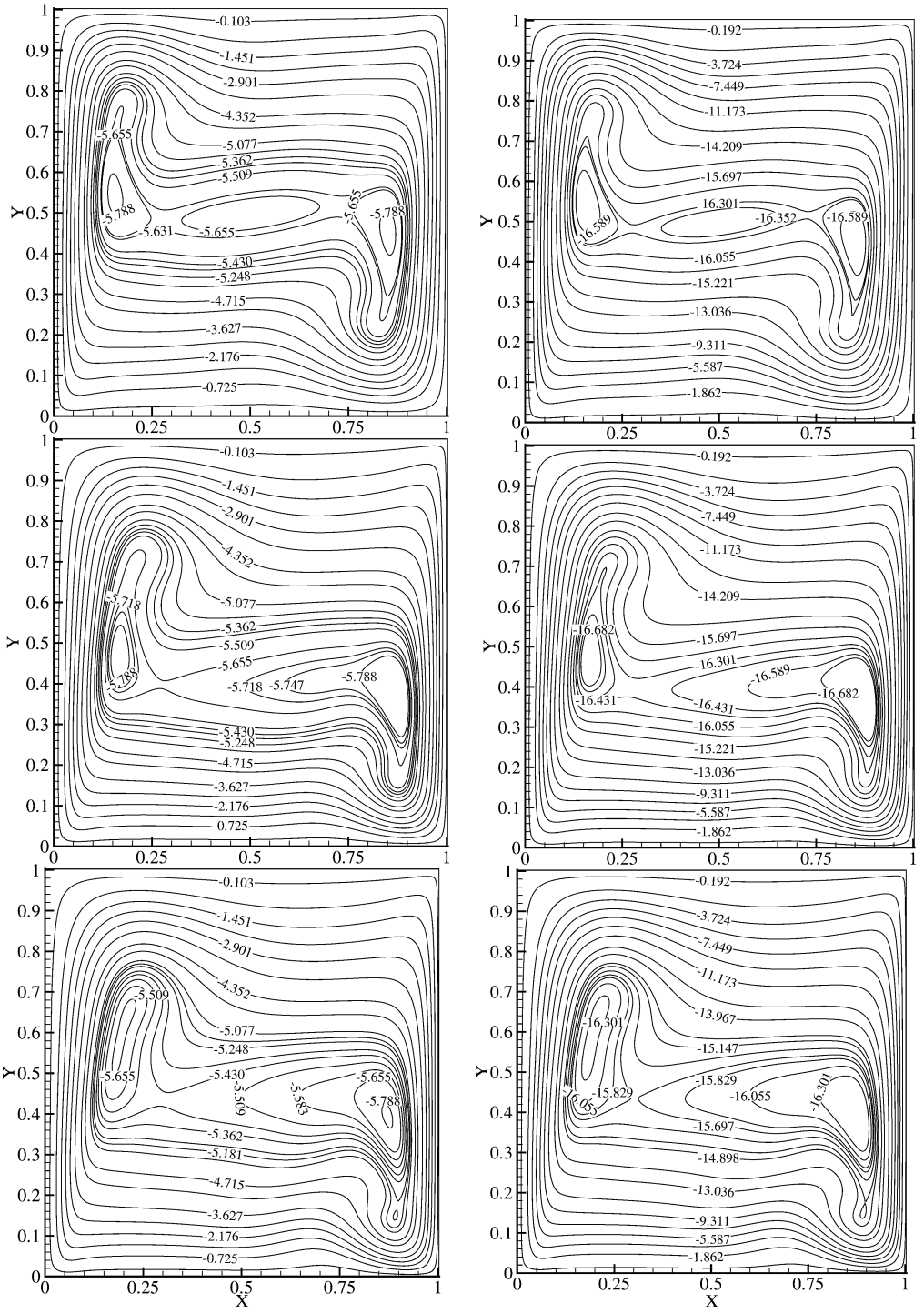

a) Incompressible-based streamfunction **b) Compressible-based streamfunction**

Fig. 9 Incompressible-based and compressible-based streamfunctions in the convecting cavity using incompressible (top) and compressible without (middle) and with (bottom) fluid property variations, $\epsilon = 0.6$.

Table 3 Required iterations and CPU times to converge to the specified convergence criterion

	Constant property cases		Variable property cases	
	CPU (s)	Iterations	CPU (s)	Iterations
Incompressible	1680	7900	N.A.	N.A.
$\epsilon = 0.01$	1186	8089	1725	8038
$\epsilon = 0.2$	1085	7409	1760	8202
$\epsilon = 0.4$	879	6004	1977	9203
$\epsilon = 0.6$	1030	7033	2089	9733

appears to be adequate resolution with grid 300×300. This is why we have presented all the results for a grid resolution of 300×300 in this section. Although Fig. 7 demonstrates the comparisons at $\epsilon = 0.6$, the current numerical experience has shown that this grid resolution would be enough fine to provide mesh independent solutions in other test cases with various ϵ's.

Figures 8 and 9 provide the isotherms and streamlines inside the convecting cavity, respectively. Figure 9 depicts the streamfunction contours for both the velocity-based streamfunction, those derived on the basis of U and V components, and the momentum component-based streamfunction, those derived on the basis of F and G components. The latter choice is to include the role of density variation in the streamfunction patterns. In other words, Fig. 9 compares the incompressible and compressible streamfunctions with each other. As is seen in this figure, there are little differences between the patterns depicted for the compressible and incompressible streamfunctions. As was shown in Fig. 6, the difference among the three taken approaches is more pronounced at $\epsilon = 0.6$ than for the lower ϵ's. Similarly, Figs. 8 and 9 also indicate that the flow behavior becomes highly asymmetric when ϵ increases. As before, the incompressible solution is unable to predict this asymmetry. Additionally, the difference between the results of the constant property and variable property is more observable in the streamfunction patterns than the isotherms.

Table 3 provides the opportunity to compare the number of iterations required to achieve the specified convergence criterion and the consequent CPU times using a grid with 100×100 resolution. The comparisons are presented for different incompressible and compressible cases with either constant-property or variable-property assumptions. Following the experience of the past investigators in this field, the residual is defined as $\mathrm{Res} = |Nu_h - Nu_c|/(Nu_h + Nu_c)$. The solution is converged if $\mathrm{Res} \leq 10^{-6}$. As is seen in this table, the number of iterations varies from 6004 for the constant-property case with $\epsilon = 0.4$ to 9733 for the variable-property case with $\epsilon = 0.6$. Although the variable-property case shows a gradual increase in the number of iterations when ϵ increases, the constant-property iterations behave chaotically. However, there are mostly minor differences in the number of iterations using different property considerations in this table. This can be considered an important advantage of the current developed algorithm and its extended formulations. The underrelaxation factors have been 0.6 for all the two velocities, pressure, and temperature calculations in our segregated algorithm. The reported CPU times are achieved on a Pentium IV computer with speed 2.6 GHz.

Conclusion

An incompressible semi-implicit-based procedure was suitably extended to solve highly thermobuoyant flowfields as compressible flows. The extended algorithm is capable of solving a wide range of density variation treatments from incompressible flow with invariant density to highly thermobuoyant flowfields with high density variation. The developed algorithm was investigated in a thermobuoyant benchmark configuration using a wide spectrum of temperature-difference parameters. As was expected, the incompressible algorithm was incapable of predicting accurate solutions in moderately to highly thermobuoyant flowfields. Fortunately, the accuracy can be recovered automatically in the developed procedure by switching to compressible flow consideration. The current results indicate that the solutions obtain serious asymmetry under symmetric geometry and boundary conditions, which definitely is contrary to both the incompressible solution and the solution of the low-temperature-difference case. The asymmetry is more pronounced for the variable-property assumption than the constant-property one under each specified condition. The current results also imply that the variable-property assumption is vital in accurate heat transfer calculations when the temperature-difference parameter is relatively high. The extended algorithm is highly robust for use as a highly thermobuoyant flow solver.

Acknowledgment

The present work was supported by the Research Center of Sharif University of Technology under Grant SUT-RC-84-4105. It is gratefully acknowledged.

References

[1]De Vahl Davis, G., and Jones, I. P., "Natural Convection of a Square Cavity: A Comparison Exercise," *International Journal for Numerical Methods in Fluids*, Vol. 3, No. 3, 1983, pp. 227–248.

[2]Gray, D. D., and Giorgini, A., "The Validity of the Boussinesq Approximation for Liquids and Gases," *International Journal of Heat and Mass Transfer*, Vol. 19, No. 5, 1976, pp. 545–551.

[3]De Vahl Davis, G., "Natural Convection of Air in a Square Cavity: A Bench Mark Numerical Solution," *International Journal for Numerical Methods in Fluids*, Vol. 3, No. 3, 1983, pp. 249–264.

[4]Doering, C. R., and Gibbon, J. D., *Applied Analysis of the Navier–Stokes Equations*, Cambridge Texts in Applied Mathematics, Cambridge Univ. Press, Cambridge, U.K., 1995.

[5]Chenoweth, D. R., and Paolucci, S., "Natural Convection in an Enclosed Vertical Air Layer with Large Horizontal Temperature Differences," *Journal of Fluid Mechanics*, Vol. 169, Aug. 1986, pp. 173–210.

[6]Choi, Y. H., and Merkle, C. L., "The Application of Preconditioning in Viscous Flows," *Journal of Computational Physics*, Vol. 105, No. 2, April 1993, pp. 207–223.

[7]Yu, S. T., Jiang, B. N., Wu, J., and Liu, N. S., "A Div-Curl-Grad Formulation for Compressible Buoyant Flows Solved by the Least-Squares Finite-Element Method," *Computer Methods in Applied Mechanics and Engineering*, Vol. 137, No. 1, 1996, pp. 59–88.

[8]Le Quere, P., Masson, R., and Perrot, P., "A Chebyshev Collocation Algorithm for 2D Non-Boussinesq Convection," *Journal of Computational Physics*, Vol. 103, No. 2, Dec. 1992, pp. 320–335.

[9]Vierendeels, J., Merci, B., and Dick, E., "Numerical Study of Natural Convective Heat Transfer with Large Temperature Differences," *International Journal of Numerical Methods for Heat and Fluid Flow*, Vol. 11, No. 4, 2001, pp. 329–341.

[10]Heuveline, V., "On Higher-Order Mixed FEM for Low Mach Number Flows: Application to a Natural Convection Benchmark Problem," *International Journal for Numerical Methods in Fluids*, Vol. 41, No. 12, 2003, pp. 1339–1356.

[11]Darbandi, M., and Hosseinizadeh, S. F., "General Pressure-Correction Strategy to Include Density Variation in Incompressible Algorithms," *Journal of Thermophysics and Heat Transfer*, Vol. 17, No. 3, 2003, pp. 372–380.

[12]Darbandi, M., and Hosseinizadeh, S. F., "A Two-Step Modification toward Implementing Compressible Source Terms in Low Compressible Flows," *Journal of Aerospace Science and Technology*, Vol. 2, No. 1, 2005, pp. 37–44.

[13]Booker, J. R., "Thermal Convection with Strongly Temperature-Dependent Viscosity," *Journal of Fluid Mechanics*, Vol. 76, Aug. 1976, pp. 741–754.

[14]Hyun, J. M., and Lee, J. W., "Transient Natural Convection in a Square Cavity of a Fluid with Temperature-Dependent Viscosity," *International Journal of Heat and Fluid Flow*, Vol. 9, No. 3, 1988, pp. 278–285.

[15]Patankar, S. V., "Numerical Heat Transfer and Fluid Flow," 2nd ed., Hemisphere, New York, 1996.

[16]Darbandi, M., and Schneider, G. E., "Analogy-Based Method for Solving Compressible and Incompressible Flows," *Journal of Thermophysics and Heat Transfer*, Vol. 12, No. 2, 1998, pp. 239–247.

[17]Leonard, B. P., "Simple High Accuracy Resolution Program for Convective Modelling of Discontinuities," *International Journal of Numerical Methods in Fluids*, Vol. 8, No. 10, 1988, pp. 1291–1318.

[18]Versteeg, H. K., and Malalasekera, W., "An Introduction to Computational Fluid Dynamics; The Finite Volume Method," Addison Wesley Longman, Reading, MA, 1995.

[19]Darbandi, M., Schneider, G. E., and Hosseinizadeh, S. F., "A Compressible Flow Solver for High Thermobuoyant Flow Fields," AIAA Paper 2004-2459, June–July 2004.

[20]Darbandi, M., and Schneider, G. E., "Application of an All-Speed Flow Algorithm to Heat Transfer Problems," *Numerical Heat Transfer, Part A*, Vol. 35, No. 7, 1999, pp. 695–715.

[21]Darbandi, M., and Schneider, G. E., "Thermobuoyancy Treatment for Electronic Packaging Using an Improved Advection Scheme," *Journal of Electronic Packaging*, Vol. 125, June 2003, pp. 244–250.

[22]Hortmann, M., Peric, M., and Scheuerer, G., "Finite Volume Multigrid Prediction of Laminar Natural Convection: Bench-Mark Solutions," *International Journal for Numerical Methods in Fluids*, Vol. 11, No. 2, 1990, pp. 189–207.

[23]Emery, A. F., and Lee, J. W., "The Effects of Property Variations on Natural Convection in a Square Enclosure," *Journal of Heat Transfer*, Vol. 121, 1999, pp. 57–62.

[24]Paillere, H., Le Quere, P., Weisman, C., Vierendeels, J., Dick, E., Braack, M., Dabbene, F., Beccantini, A., Studer, E., Kloczko, T., Corre, C., Darbandi, M., and Hosseinizadeh, S. F., "Modelling of Natural Convection Flows with Large Temperature Differences: A Benchmark Problem for Low Mach Number Solvers. Part 2," *ESAIM: Mathematical Modelling and Numerical Analysis*, Vol. 39, No. 3, 2005, pp. 617–621.